Journal of Applied Fluid Mechanics, Vol. 12, No. 5, pp. 1547-1561, 2019.
Available online at www.jafmonline.net, ISSN 1735-3572, EISSN 1735-3645.
DOI: 10.29252/jafm.12.05.29648

An Experimental Investigation of a Passively Flapping Foil in Energy Harvesting Mode

M. N. Mumtaz Qadri[1†], A. Shahzad[1], F. Zhao[2] and H. Tang[2]

[1] *Department of Aerospace Engineering, College of Aeronautical Engineering, National University of Sciences & Technology, Islamabad, 44000, Pakistan*
[2] *Department of Mechanical Engineering, The Hong Kong Polytechnic University, Hong Kong, China*

†*Corresponding Author Email: m.n.mumtaz.qadri@cae.nust.edu.pk*

(Received September 18, 2018; accepted December 26, 2018)

ABSTRACT

Energy extraction through flapping foils is a new concept in the domain of renewable energy, especially when the system is fully driven by incoming free-stream flow, a phenomenon known as flow-induced vibration. To investigate this concept, a water tunnel test-rig was designed and fabricated, where a flat plate foil made from plexiglass performs two-degrees of freedom pitch and plunge motion under the influence of incoming water flow. For this study a power-takeoff system was not introduced, hence energy harvesting performance was evaluated through real-time force and motion measurements with the help of sensors. The energy harvester performed self-sustained flapping motions when the free-stream velocity reached a threshold value, known as the cut-off velocity, which for this test-rig is 0.40 m/s (without sensors) and 0.50 m/s (with sensors). To support these self-sustained flapping motions, inertial mass blocks were placed to provide the necessary inertia especially when the flat plate foil performed the pitching or stroke reversal action. Different inertial mass units (m_{ib} = 0.45, 0.90 & 1.35 kg/block) were tested to analyze their effect on the flat plate foil kinematics and its energy harvesting performance. Other parameters such as pitching amplitude (θ_o = 30˚, 43˚ & 60˚) and free-stream velocity (U_∞ = 0.57 m/s, 0.65 m/s and 0.78 m/s) were varied at fixed pivot location (x_p = 0.65 chords (c)) to augment the varying inertial mass unit study. In the first section at fixed m_{ib} of 0.45 kg/block and x_p = 0.65c from leading edge, energy harvesting performance ($\overline{C}_p$ & η) was observed to increase with increase in pitching amplitude, while it degraded as the free-stream velocity increased. Best energy harvesting performance of η = 52.5% and $\overline{C}_p$ = 1.124 was achieved with m_{ib} = 0.45 kg/block, θ_o = 60˚ and U_∞ = 0.57 m/s. Varying m_{ib} also had a considerable effect on the energy harvesting performance of the test-rig, where the m_{ib} = 0.90 kg/block case showed a 36.5% and 21.13% decline in performance compared to the m_{ib} = 0.45 and 1.35 kg/block cases, respectively at θ_o = 60˚ and U_∞ = 0.57 m/s. This shows that the energy harvester is sensitive to changes in inertial loads, affecting the force-motion synchronization which eventually affects its performance.

Keywords: Fluid-structure interaction; Bio-inspired energy harvesting; Leading edge vortex; Flow-induced passive flapping motion.

NOMENCLATURE

b	hydrofoil span	*DoF*	degrees of Freedom
c	hydrofoil chord length	m_{ib}	inertial mass unit mass
C_{ph}	coefficient of power due to plunging motion	η	energy extraction efficiency
$C_{p\theta}$	coefficient of power due to pitching motion	U_∞	free-stream velocity
C_p	coefficient of total power	x_p	distance from L.E as a ratio of chord length
$\overline{C}_p$	mean coefficient of power	θ_o	pitching amplitude w.r.t horizontal direction free-stream velocity (in degrees)
C_h	coefficient of hydrodynamic lift force		
C_θ	coefficient of hydrodynamic moment		
d	swept distance		

1. INTRODUCTION

With drastic increase in world population, the demand for sustainable energy solutions is on the rise. This has led to the growing commitment at the global level to not only limit the greenhouse effects due to the excessive use of fossil fuels but also encourage the development and implementation of energy harvesting solutions with its source driven from renewable resources, provided by nature in abundance. Examples include; sunlight, wind, tides, waves and geothermal energy, providing a clean and replenishable source of energy. Energy extraction from winds and tides is a very attractive initiative and has been in practice for many decades, which has been possible via the introduction of turbine-based energy harvesting devices such as Vertical Axis Water Turbines and Horizontal Axis Water Turbines. However, a promising concept has arisen of extracting energy from wind or tides through devices whose working principle is "*bio-inspired*". Unlike these conventional turbines, bio-inspired energy harvesting devices are; environmentally friendly due to low tip speed reducing the impact on aquatic animals' navigation, they are structurally robust unlike the rotating blades which suffer from centrifugal stress, bio-inspired energy harvesters have a rectangular cross-section and swept distance for a single device is wide and shallow, thus allowing for larger systems to be installed in shallow water sources (Yonghui Xie *et al.* (2014)).

The concept of energy harvesting through flapping motion was first introduced by McKinney & DeLaurier (1981), where they studied the feasibility of a wind energy extraction device consisting of a foil undergoing coupled pitching and plunging motion through theoretical and experimental techniques. They observed that the output power and efficiency achieved by their system may be comparable to that of a rotary turbine. Studies have shown that the bio-inspired energy harvesting device can be divided into three categories based on its motion modes activation mechanism; fully active (motion modes' kinematics are prescribed), semi-active (one of the motion modes is prescribed while the other is flow-driven) and fully passive (both motion modes are fully flow driven or flow induced).

Extensive work has been carried out on fully active and semi-active systems (Kinsey & Dumas (2008), Abiru & Isogai (2012), Simpson *et al.* (2008 a, b), Ashraf *et al.* (2011) etc), both experimentally and computationally. In the case of fully active energy harvesting systems, different kinematics can be programmed for pitching and plunging motion modes, allowing the foil to behave according to the assigned kinematics rather than depending on the flow conditions, hence focusing on the parametric domain of the bio-inspired energy harvesting device. Through sinusoidal pitch and plunge motions of a NACA0015 foil at Re = 1100, Dumas & Kinsey (2006) found efficiencies as high as 34% at x_p = 0.33c and pitch-plunge phase difference of 90˚. Kinsey and Dumas (2008) also found for a range of reduced frequency (k) = 0.75-1.13 to be good for power extraction for sinusoidal flapping wing turbines. Xiao *et al.* (2012) also computationally investigated different methods to improve the energy extraction efficiency of a flapping foil through pitch motion control. Ashraf *et al.* (2011) performed simulations of fully prescribed plunge and pitch motions of a NACA0014 foil at $Re = 2.0 \times 10^4$ and φ = 90˚. Through surrogate assisted evolutionary optimization algorithm, he searched for optimum combinations of four parameters and found the best performance in the range of k (reduced frequency) = 1.02-1.06, h (plunging amplitude) = 0.81c-0.93c, θ_o = 80˚ and x_p = 0.44c-0.46c, with the highest efficiency found at 33.5%.

In semi-active flapping foil energy harvesting systems, mostly the pitching motion is prescribed, while the plunging motion is flow induced. Shimizu *et al*. (2008) designed and computationally analyzed a semi-passive flapping system with a NACA0012 foil with sinusoidal pitching motion and flow-induced plunging motion. They also observed the significance of the timing and formation of LEV during the flapping motion, causing it to increase the mean power coefficient by 36.6%. Hisanori & Akira (2012), through semi-passive techniques on a NACA0015 foil demonstrated energy extraction through flapping motions where the plunge motion was supported by a leaf spring. They also studied the impact of perpendicular distance between two flapping foils in bi-plane arrangement with cascade foil. Isogai & Abiru (2012) studied the power generation and efficiency of a multi-foil configuration of a 2D NACA0015 foil at Re = 38,000 using the analytical method based on linear potential aerodynamic theory and numerical simulation on N-S equation.

Numerous studies have been carried out on fully active and semi-active energy harvesting flapping wing systems, mostly computational. By programming different kinematic parameters, more focus has been put on the parametric study of energy harvesting through flapping motions rather than observing the effect of flow conditions on the harvester performance. Such is not the case for a fully passive flapping foil power extractor, a category which needs more attention. The system's activation mechanism is fully flow-induced and slight changes in the flow modifies the force generation. As mentioned earlier, McKinney & DeLaurier (1981) first demonstrated the concept of energy harvesting through their passively actuated flapping wing. Peng & Zhu (2009) computationally demonstrated a flapping foil driven by flow instability at Re = 1000, with the foil modeled with torsional spring and linear damper. Poirel *et al.* (2006, 2008 & 2011) did experiments on an aeroelastic phenomena known as flutter, which could be used as an energy harvesting phenomenon. The setup consisted of a 2-DoF system with a spring mounted rigid NACA0012 wing moving in translation and rotation. Impact of free-stream, elastic axis position and structural stiffness on the foil's limit cycle oscillations were investigated at $Re = 4 \times 10^4$ to 1.4×10^5. Kinsey *et al.* (2011) also performed experiments by designing and implementing a 2-kW flapping foil energy harvester

prototype on the pontoon boat and tested in a lake, with design features based on his earlier computational studies (Dumas & Kinsey (2006) and Kinsey & Dumas (2008)). The most prominent yet simple design to mimic a flapping motion under the influence of incoming free stream flow was introduced by Platzer *et al*. (2009). The device did not include any complex mechanisms such as those in the experimental setups of Poirel *et al*. (2006), Kinsey *et al*. (2011) and McKinney & DeLaurier (1981), to induce any kind of pitch-plunge phasing or to create a specified motion profile.

The hydrofoil plunges on a guide rail and rotates about a pivot axis aft of the mid-chord position. This ensures that the foil is statically unstable and deflects to a high pitch angle until it is stopped by a mechanical restraint in the form of a pitch limiter.

This drives the foil due to the lift force on the hydrofoil, and the foil flips back at the end of the stroke by a moment arm on the foil contacting another mechanical restraint or a plunge limiter. In a multi-foil configuration, the downstream system does not rely on the upstream system to start (self-starting).

From the literature review, we have observed that most of the studies have focused on fully active and semi-active systems, while the research on fully passive systems is in its infancy. Computational studies provide some understanding of the flow physics; however, an experimental campaign shows a detailed and realistic picture of the behavior of flapping foils and their energy harvesting performance when subjected to actual fluid flow. Fluid-structure interaction and kinetic analysis through experiments of a fully passive foil energy harvester are also not available. This motivates us to carry out detailed experiments to investigate and study the concept of a "*fully passive*" flapping foil energy harvester and to design and fabricate a test-rig where flapping motions are fully flow induced and not dependent on any kind of mechanisms. This will allow us to observe how the hydrofoil responds to the flow conditions it is subjected to in an open channel environment. In this research paper we will discuss the methods to make the test-rig viable so that it can perform sustainable flow induced flapping motions, for which the introduction of different inertial mass units (m_{ib} = 0.45 kg, 0.90 kg and 1.35 kg) and their effect on energy harvesting performance and flapping foil kinematics will be discussed. We will also explain the effect of other parameters such as pitching amplitude (θ_o = 30˚, 45˚ and 60˚) and free-stream velocity (U_∞ = 0.57 m/s, 0.65 m/s and 0.78 m/s) on the energy extraction performance of the system.

2. TEST MODEL AND DATA ACQUISITION

2.1 Test Model Setup

The experiments were conducted in a closed-circuit water channel, having a cross-sectional area of 0.3 m × 0.6 m and length of 2.0 m. The experimental campaign was conducted in an open channel configuration by removing the top acrylic panel and placing the test-rig on top of the test section.

Our test-rig design is inspired from Platzer & Bradely (2009) patent design, with its working principle discussed in the previous section. Semler (2010) conducted simple experiments to fully understand the mechanism of the device introduced by Platzer & Bradely (2009). Fig. 1 (a) shows the model of the test-rig, while Fig. 1 (b) shows the pitching limiter setup. The system is free of any complex mechanisms and both motion modes (plunge and pitch) are influenced by the incoming flow. The hydrofoil is a rigid flat plate, made of plexiglass with a rectangular planform of chord length (c) 140 mm, span (b) 200 mm and thickness (t) 5 mm. It is mounted in a vertical cantilevered arrangement at x_p = 0.65c, while the distance between the plunge limiters (201.5 mm) is fixed. To maintain the two-dimensionality of the study, endplates on the top and bottom part of the foil are arranged with a clearance of approximately 3.5 mm, to reduce end effects. The top endplates are made from black acrylic to avoid background reflection and arranged to introduce a slit to ensure un-interrupted plunging motion.

A laser-induced fluorescent (LIF) flow visualization system was used to qualitatively visualize the flow around the flapping foil. To achieve this, a small hole of 3.5 mm (diameter) at about 0.25c from leading edge (L.E) was drilled at half span from the top wing root (Fig. 2) to accommodate the rubber tube. A 1.5 mm diameter hole is drilled through from the L.E at mid span to connect with the 3.5 mm diameter vertical cavity (Fig. 2) while a 1 mm diameter pinhole is drilled, perpendicular to the span, through the 1.5 mm diameter horizontal channel allowing the fluorescent dye to exit through the pinholes (Fig. 2). The dye tracer used in the LIF experiments were fluorescent poster colors from Pental, which were mixed and stored in a 1 L beaker and then extracted using a 50 mL syringe. The syringe was connected to the rubber tubes which were attached carefully to the vertical cantilevered shaft and the end of the tube inserted and secured into the 3.5 mm diameter hole on the hydrofoil model. Due to the unavailability of a syringe driver, the dye tracer was inserted manually but carefully (equal constant pressure applied while operating the syringe) to the tube connected to the syringe. To illuminate the dye tracer, a solid state 532 nm green laser with attached optics and with a maximum power of 10.84 W in the continuous mode was set at the mid-span of the foil, as shown in Fig. 3.

2.2 Data Acquisition

To measure the forces and torque of the flapping foil, we chose a six-component ATI Mini-40 IP68 Force/Torque sensor. The sensor has a force measuring range of ±80 N in both x and y directions and ± 4 N-m for torque about its z-axis. The sensor is attached between the vertical cantilevered shaft as shown in Fig. 1 (a). The force sensor's z-axis is oriented making it normal to the pitch-plunge plane as shown in Fig. 3. For pitching and plunging motion

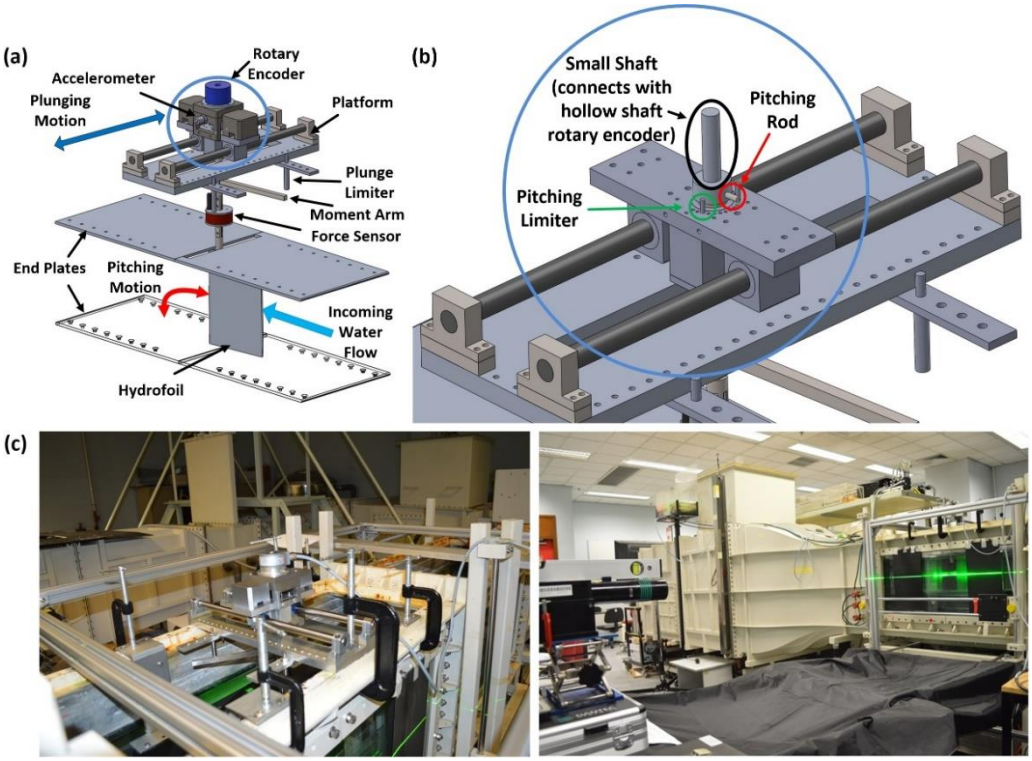

Fig. 1. (a) Schematic of the experimental setup of a passively oscillating energy harvester with sensors, hydrofoil and endplates installed, (b) Expanded view of small platform on guide rail showing the pitching limiter mechanism, (c) Pictures of experimental test-rig and water tunnel.

measurements, a Kubler Sendix 5020 Push-Pull rotary incremental encoder and Type 4382 uni-axis charge accelerometer from Bruel & Kjaer were used respectively (also shown in Fig. 1 (a)).

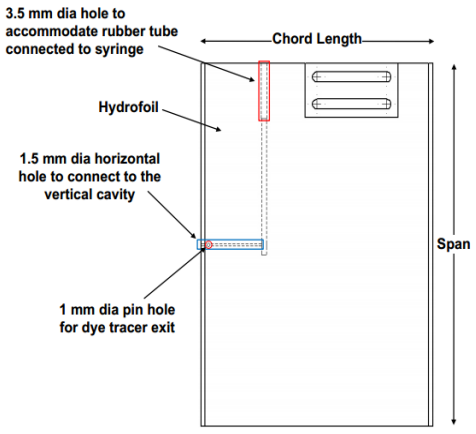

Fig. 2. Schematic of the arrangement of different holes and cavities to accommodate the rubber tube into the hydrofoil and allow the dye tracer to exit the pin hole situated near the leading edge of the hydrofoil.

The rotary encoder is a hollow shaft encoder, which has a through hole in the center, allowing it to be coupled with part of the vertical cantilevered shaft shown in Fig. 1 (b). This allows the encoder to measure the angular displacement when the hydrofoil (at the end of the vertical cantilevered shaft) is subjected to the incoming free-stream flow. The accelerometer used here is a contact-less sensor; meaning that it is installed on the test-rig in a way that it will in not alter or interfere with the flapping foil motion. The sensor is an analog sensor and needs and is connected to the data acquisition system through a signal conditioner, as shown in Fig. 4, converting the acceleration signal to displacement.

All sensors are connected to a computer via a National Instrument (NI) cDAQ 9174 Compact DAQ chassis which houses three different DAQ modules interfaced with the sensors: two analog input modules (NI 9220 for the ATI force sensor and NI 9215 BNC for the charge accelerometer) and one digital input module (NI 9411 for the rotary incremental encoder) as shown in Fig. 4. The accelerometer was connected to the input section of channel 1 of the charge amplifier. Since the amplifier was set to double integration, the displacement signal with a gain value set at 1 V/m on the conditioning amplifier was sent to the NI 9215 BNC from the conditioning amplifier's output section of its channel 1. Sampling frequency was set at 2000 Hz for all sensors in the LabView 2014 Virtual Instruments (VI), which is adequate to give us enough data points to post-process. Two VIs programs were designed for data acquisition from the sensors. One program was responsible for force and torque data acquisition

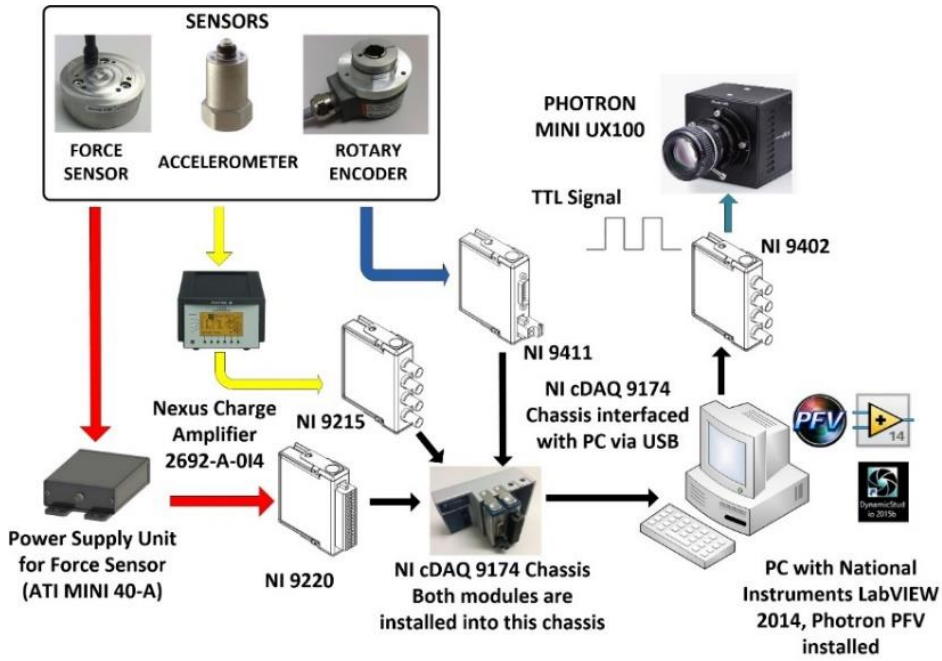

Fig. 3. Experimental setup for qualitative assessment of flow structures around a flapping foil in energy extraction mode. The dye used is fluorescent and is illuminated by the laser positioned at midspan of the oscillating flat plate.

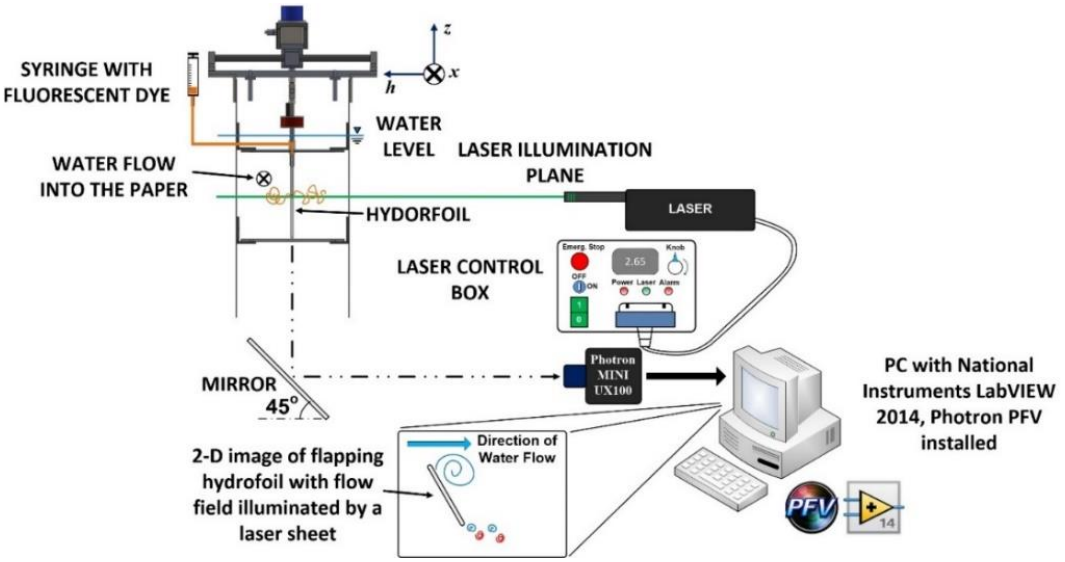

Fig. 4. Schematic showing interfacing between sensors and their respective DAQ modules, installed in a single NI cDAQ 9174 chassis. The chassis is connected to the PC via USB cable, which has LabVIEW 2014 installed.

from the force sensor while the second program for acquisition of displacement signals from the linear and rotary sensors. The second program also consisted of a module which could send TTL signals via NI 9402 BNC to the camera. Both VI were synchronized and to achieve this the force-torque data VI was made as the Master program while the displacement VI was made as the Slave. Upon activation of the Master VI, both programs would start and simultaneously will receive raw sensor data in real-time and would send TTL signals via the NI 9402 BNC output digital module.

For image acquisition, a Photron FASTCAM Mini (UX100) high speed camera was used (Fig. 4). It has an internal capacity of 16GB with a frame rate of 4000 frames per second at a full resolution of 1024 × 1280 pixel. The camera has BNC input terminals which can be used to activate its image acquisition upon receiving a TTL signal, which was achieved through the NI 9402 BNC digital module (Fig. 4). Since the VI programs were synchronized, upon the activation of the program, the camera receives the TTL signal to acquire the images while the LabView program simultaneously starts to receive the raw data

from the sensors. The camera software used for the image acquisition for qualitative analysis is the Photron FASTCAM Viewer (PFV) v3. The frame rate was set to 125 fps with shutter speed at 1/640 sec and image resolution of 1024 × 1280 pixels, which is approximately 70 seconds of image data.

2.3 Equations to Determine Energy Harvesting Performance

Figure 5 shows the orientation of the force sensor coupled with the hydrofoil. The positive *x* and *y*-axis as set by the force sensor manufacturer can be seen in the figure, where the *x*-axis and the *y*-axis are parallel and perpendicular to the chord line respectively. To calculate the lift or vertical force acting on the hydrofoil, the force data from the sensor ($F_{x'}$ and $F_{y'}$) are decoupled using simple trigonometric and algebraic expression as shown in Equation 1:

$$F_V = F_{y'}cos\theta + F_{x'}sin\theta \quad (1)$$

$$F_H = F_{y'}sin\theta - F_{x'}cos\theta \quad (2)$$

where F_V and F_H are the vertical (lift) force and horizontal (drag) forces which are parallel and normal to the plunging motion direction, respectively. As mentioned, the dynamic force and moment data acquired from the sensor are synchronized with the motion sensors and the acquired camera images, hence the instantaneous angular displacement data (θ) from the rotary encoder was used to calculate F_V and F_H using Equation 1. The *z*-axis of the force sensor was already perpendicular to the pitch-plunge plane and parallel to the vertical cantilevered shaft, hence no such transformation of moment (T_Z) data was required.

Before this process of resolving forces, the force-torque ($F_{x'}$ and $F_{y'}$) and linear displacement data from the sensors were passed through a low pass filter with a cut-off frequency of 10 Hz to remove any noise or high-frequency components without sacrificing the profile and amplitude of the data. Using an in-house Matlab code, the linear and angular displacement data were used to calculate the linear and angular velocities and acceleration ($\dot{h}(t), \ddot{h}(t)$ and $\dot{\theta}(t), \ddot{\theta}(t)$). A total of nine parameters including both measured and calculated parameters ($F_{x'}$, $F_{y'}$, T_Z, $h(t)$, $\dot{h}(t), \ddot{h}(t)$, $\theta(t)$, $\dot{\theta}(t), \ddot{\theta}(t)$) were then phase-averaged (over 35 cycles).

In this setup, the forces measured consisted of two components: (i) the hydrodynamic force and (ii) inertial force. The energy extraction performance parameters were calculated using the hydrodynamic force and moment data. Therefore, the inertial forces were subtracted from the measured force and moment data to obtain the hydrodynamic force and moment values. The equations are as follows;

$$F_{inertial} = m\ddot{h}(t) \quad (3)$$

$$F_h = F_V - F_{inertial} \quad (4)$$

where m is the mass of the hydrofoil and the small vertical shaft underneath the force sensor (= 0.20 kg), $\ddot{h}(t)$ is the linear acceleration, $F_{inetial}$ is the linear inertial force and F_y is the net vertical hydrodynamic force (hydrodynamic lift force). For the net hydrodynamic moment calculation (Equation 3), the same principle was applied as with the calculation of the hydrodynamic lift force;

$$T_{Z-inertial} = I_Z\ddot{\theta} \quad (5)$$

$$T_\theta = T_Z - T_{Z-inerital} \quad (6)$$

$$I_Z = I_{CM} + mx_{c-piv}{}^2 \quad (7)$$

where I_Z is the mass moment of inertia, which is also dependent on the pivot location where the vertical shaft is attached as given in Equation 4 where I_{CM} is the moment of inertia with respect to hydrofoil's mid-chord and $x_{c\text{-}piv}$ is the distance between the pivot location and the mid-chord of the hydrofoil, $\ddot{\theta}(t)$ is the angular acceleration, $T_{Z\text{-}inertial}$ is the inertial moment and T_θ is the net hydrodynamic torque about the *z*-axes (parallel to the vertical cantilevered shaft).

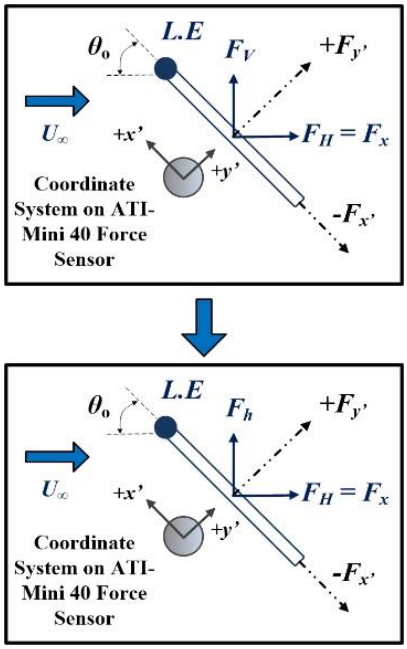

Fig. 5: Definition of force vectors on the hydrofoil. $F_{x'}$ and $F_{y'}$ are forces parallel and normal to the hydrofoil which are measured by the force sensor directly. F_H and F_V are horizontal and vertical forces which are normal and parallel to the plunging direction while F_h is the hydrodynamic lift force, respectively. 'L. E' represents the leading edge of the flat plate, which is marked by a relatively large color filled circle at one end of the wing.

The phase-averaged parameters are then used to evaluate the system performance of the flapping foil energy harvester including; instantaneous total extracted power (P, C_p), instantaneous extracted power due to plunging motion (P_h, C_{ph}), instantaneous power due to pitching motion (P_θ,

$C_{p\theta}$), time-averaged power and coefficient of power ($\bar{P}$, $\bar{C}_p$), efficiency (η) and force-torque parameters (F_y, C_h, T_θ, C_θ), by applying equations 8 to 13.

$$P = F_h\dot{h} - T_\theta\dot{\theta} \tag{8}$$

$$P = P_h - P_\theta \tag{9}$$

where, $\dot{h}$ is the plunging velocity and $\dot{\theta}(t)$ is the pitching velocity, F_h is the hydrodynamic vertical force or net lift force, T_θ is the hydrodynamic moment or net torque. To calculate the coefficient of power (C_p) and mean coefficient of power ($\bar{C}_p$), the following equations are as follows:

$$C_p = C_h\frac{\dot{h}}{U_\infty} + C_\theta\frac{\dot{\theta}c}{U_\infty} \tag{10}$$

$$C_p = C_{ph} + C_{p\theta} \tag{11}$$

$$\bar{C}_p = \frac{1}{T}\int_t^{t+T} C_p(t)\,dt = \bar{C}_{ph} + \bar{C}_{p\theta} \tag{12}$$

where, C_h and C_θ are the coefficients of vertical hydrodynamic force and hydrodynamic moment respectively. The efficiency (η) of the energy extraction is measured as the ratio of time-averaged power output to the available power in the flow through the frontal area of the foil;

$$\eta = \frac{\bar{P}}{\frac{1}{2}\rho U_\infty^3 bd} = \bar{C}_p\frac{c}{d} \times 100 \tag{13}$$

where, d is the distance swept by the foil, which is set to 0.3 *m*. Since the ratio of the efficiency to the mean power coefficient is constant for a given c and d, discussing only one of them is enough.

3. RESULTS AND DISCUSSION

3.1 Methods to Ensure Test-Rig Sustainability

As a first step, we performed various tests to ensure that the test-rig would be able to perform sustainable and viable flapping motions when induced to incoming flow. During our preliminary experiments, we observed that under different test conditions, which included varying inertial mass and free stream velocities, the flat plate foil was able to perform plunging motion at maximum pitching angle and stroke reversal under the influence of hydrodynamic forces. The inertial blocks of appropriate mass would be attached on top of the aluminum block resting on the guide rail as shown in Fig. 1. The test-rig was tested in two different hardware configurations; one without sensors attached and one with sensors attached. Furthermore, two different lengths of the vertical cantilevered shaft were also taken into consideration; one long (274 mm) to accommodate the force sensor in between and one short (186 mm) as shown in Figure 6. All the above-mentioned configurations, shaft length and inertial mass unit determined the cut-off water velocity ($U_{\infty\text{-cutoff}}$) of the test-rig, which is defined as the water velocity at which the hydrofoil performs sustainable flapping motions without any external help.

Initial tests revealed that the configuration involving a shorter shaft of about 186 mm (from top till upper wing tip) required less inertial block mass (< 150g per block) to perform self-sustainable flapping motions for energy harvesting. With a rotary encoder coupled to the top of the vertical shaft, the inertial block mass increased to about 250 g (per block). The increased mass was because the screw in the rotary encoder used to couple it with the vertical shaft was tightened to an extent that it allowed the shaft to rotate by not requiring high hydrodynamic force. According to the sensor's manual, the minimum torque required was about 0.5 N-m. This way it was also possible to acquire good pitching motion data without compromising the flapping motion. The cut-off speed acquired for this configuration was approximately 0.37 m/s.

Although the rotary encoder could be used with any length of vertical shaft, the force sensor had to be accommodated, which was possible in a vertical shaft longer than shown in Fig. 6 (b). Through careful adjustments and taking into consideration the water height in the water tunnel for future experiments (470 mm from bottom tunnel wall), the shaft's length was increased to about 274 mm, which helped accommodate the moment arm and the force sensor. However, by increasing the shaft length, the smaller mass blocks (< 250 g) could not be used for the foil to perform self-sustainable flapping motions. Hence, larger inertial mass blocks (>250 g) were taken into consideration. For the longer shaft but with no rotary encoder coupled to it, inertial mass blocks of approximately 300 g/block were sufficient, while with the rotary encoder about 400 g/block. This also increased the cut-off velocity of the system to about 0.50 m/s (with all sensors and longer vertical cantilevered shaft).

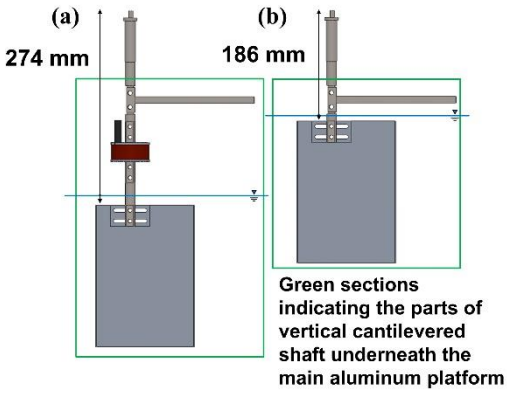

Fig. 6. Schematic of vertical cantilevered shaft used in experiments, (a) Current configuration of the vertical cantilevered shaft including the force sensor attached with a custom-made flange and (b) initial configuration of the vertical cantilevered shaft used in our preliminary experiments to determine the suitable setup for the test-rig to perform self-sustained flapping motions.

It is to be kept in mind that the flapping motion performed by this test-rig in energy extraction mode is 2-DoF (plunging and pitching motion). Although, once the hydrofoil was at its maximum pitching amplitude (determined by the pitching limiter as shown in Fig. 1 (b)) it could perform pure plunging

motion because of incoming free-stream velocity applying hydrodynamic force on the foil regardless of the presence or absence of inertial mass and/or other configurations. However, when the foil reached the end of the stroke, i.e. the moment arm touching the plunging limiter, it would only perform stroke reversal if the foil had gained enough momentum and it had the necessary mass to push it. If the moving aluminum platform didn't have enough inertia, the stroke reversal would not be initiated, and the flapping motion would not be completed; making the test-rig not sustainable. Hence, the inclusion of appropriate inertial mass blocks was an important factor to tackle this problem under the kinematic range in which the experiments were to be conducted (details in the next section). Furthermore, the inertial mass units also serve as a mechanical load installed on the test-rig due to which the foil would perform differently coupled with other geometric and kinematic parameters, which will be discussed in Section 3.3.

Three different inertial mass block units have been tested and their performance comparison has been investigated in detail and two of each kind are used during an experiment to provide equal mass distribution on the small aluminum block on the guide rail. The smallest is about m_{ib} = 0.45 kg/block, the medium or baseline is about m_{ib} = 0.90 kg and largest is about m_{ib} = 1.35 kg/block. The smallest one is about 50 g higher than the threshold required for sustainable flapping motions by the test-rig configuration including all sensors and long vertical shaft. The other two were selected by linearly increasing the mass by 450 g. Effect of pitching amplitude (θ_o = 30˚, 43˚ and 60˚) and free stream velocity (U_∞ = 0.57 m/s, 0.65 m/s and 0.78 m/s) on energy harvesting performance at a fixed pivot location (x_p = 0.65c) and inertial mass unit will also be discussed in this paper.

The reason for choosing these free-stream velocity values, which are also in a very narrow range is not only due to the cut-off free stream at 0.50 m/s but also through our preliminary testing we observed that at very high-water speeds (U_∞ > 0.85 m/s), different parts of the test-rig were getting damaged. The most affected part was the pitching limiter, which later was manufactured using stainless steel. Therefore, no parametric studies were conducted beyond U_∞ = 0.80 m/s. For pitching amplitude values, although our test-rig could accommodate till 87˚, but due to the plunge limiter to the other plunge limiter distance set at 201.5 mm and the wall to wall distance of the water tunnel facility at 300 mm, pitching amplitude study could not go beyond 60˚ to avoid glass wall strikes by the foil. Therefore, three pitching amplitude with approximately 15˚ increments (30˚, 43˚ and 60˚) were chosen for experiments.

3.2 Effect of Free-Stream Velocity & Pitching Amplitude at Fixed Inertial Mass (m_{ib} = 0.45 kg)

In this section, we will investigate the effects of varying pitching amplitude and free-stream velocity at a fixed pivot location and inertial mass block on the energy harvesting performance of this test-rig. For now, the analysis will be done on m_{ib} = 0.45 kg/block inertial mass system and in Section 3.3 we will compare the energy harvesting performance of the test-rig when the inertial mass is increased linearly. Figure 7 shows the energy harvesting performance ($\bar{C}_p$) of the test-rig at three different pitching amplitudes and three different free-stream velocities in each pitching amplitude group. The stacked columns also show the ratio of contribution by both plunging motion (blue) and pitching motion (red) to the total energy harvesting from incoming flow.

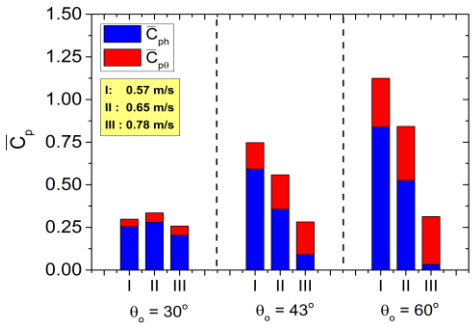

Fig. 7. Stacked column configuration of $\bar{C}_p$ at different free-stream velocities in each pitching amplitude group for a test-rig configured at x_p = 0.65c and m_{ib} = 0.45 kg/block. The blue bars represent the contribution by the plunging motion ($\bar{C}_{ph}$) and red bars by the pitching motion ($\bar{C}_{p\theta}$) to the total energy harvesting at each free stream velocity.

From Fig. 7 we observe that at fixed free-stream velocity and varying pitching amplitude we observe an increase in energy harvesting performance. This increase in performance is more sensitive at lower free-stream velocities (U_∞ = 0.57 and 0.65 m/s), while at U_∞ = 0.78 m/s the increase is very gradual. While for each pitching amplitude especially at θ_o = 43˚ and 60˚, with increase in free-stream velocity the energy harvesting performance of the flat plate foil decreases. To understand these trends, it is important to analyze the behavior of both force and motion components, through which the performance of the system is determined. The synchronization between such force and motion parameters plays an important role in determining the energy harvesting performance of the system, which are sensitive to geometric and kinematic changes.

Figure 8 shows the C_p plots and Fig. 9 shows the plunging and pitching parameters (force, motion and energy) of a flat plate foil with varying free-stream velocity at θ_o = 43˚, m_{ib} = 0.45 kg/block and x_p = 0.65c. As observed in Fig. 7, the performance of the flat plate foil decreases while the free-stream velocity increases, which could also be seen in Fig. 8. Furthermore, the red region marked in Fig. 8 shows the area where the energy is lost by the system during the flapping cycle rather than energy harvested from the incoming free-stream. This energy expenditure is prominent for U_∞ = 0.65 and 0.78 m/s cases as observed in Fig. 8. It is important

to note that C_p is the sum of C_{ph} and $C_{p\theta}$, hence the cohesion between the plunging and pitching forces with their respective velocities is an important factor, which will be discussed in the following paragraphs.

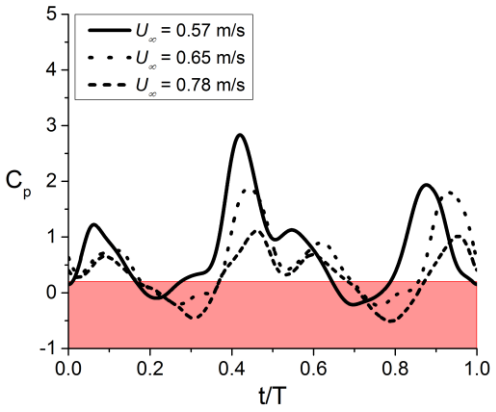

Fig. 8. C_p plots at different free-stream velocities for a test-rig configured at θ_o = 43˚, x_p = 0.65c and m_{ib} = 0.45 kg/block. The lightly shaded red region shows the area of energy expenditure by the system rather than extracting energy from the free-stream.

Figure 9 (a) represents the hydrodynamic force (C_h), velocity ($\dot{h}/U_\infty$) and power extraction (C_{ph}) due to plunging motion in blue color with different line styles, while Fig. 9 (b) shows the hydrodynamic torque (C_θ), velocity ($\dot{\theta}c/U_\infty$) and energy harvested ($C_{p\theta}$) due to pitching motion for different free-stream velocities. In each plot in Fig. 9 portions of the flapping cycle are marked with gray boxes. These boxes represent the time for pitching amplitude to remain constant set by the pitching limiter (in this case θ_o = 43˚), which occurs during the pure plunging phase of the flapping cycle. The white areas represent the stroke reversal or pitching motion in which the flat plate foil goes from $+\theta_o$ to $-\theta_o$ or vice versa. The first gray box in every plot is when the foil is plunging at $+\theta_o$ and the second gray box is when the foil is plunging at $-\theta_o$.

From Fig. 8 and Fig. 9 we can observe that C_p plots follow their respective C_{ph} profiles, while $C_{p\theta}$ has peaks at two instants during the flapping cycle. The two peaks in each of the plots in Fig. 9 (b) occur during the ending phase of the stroke reversal, when the flat plate foil touches the pitching limiter. The strike at the pitching limiter allows the force sensor to record that as a spike in the measured torque and forces. During the remainder of the flapping cycle since the flat plate foil is constant at maximum pitching amplitude, the angular velocity remains zero due to which $C_{p\theta}$ remains approximately zero. It can also be deduced that most of the energy extracted from the incoming free-stream flow is due to the plunging motion of the foil, while pitching motion only contributes when the foil completes its stroke reversal. Contributions from both motion modes can also be seen in Fig. 7. With increase in free-stream velocity for θ_o = 43˚, the flapping frequency of the flat plate foil increases (0.648, 0.742 and 0.847 Hz for U_∞ = 0.57, 0.65 and 0.78 m/s, respectively). The high flapping frequency allows the flat plate foil to traverse the constant pitching amplitude plunging motion faster due to which the plunging motion has less time to contribute towards the total energy extraction.

At U_∞ = 0.57 m/s, C_p graph (Fig. 8) has multiple high peaks and remains positive for almost the whole flapping cycle, which is due to the good synchronization achieved by the hydrodynamic lift force and linear velocity, as shown Fig. 9 (a-i). Synchronization between the two parameters corresponds to the same signs remaining the same during the flapping motion. As a result, positive energy extraction due to plunging motion was achieved as seen in Fig. 9 (a-i). From Fig. 9 (a-ii), due to non-sinusoidal motion of the hydrofoil, the angular velocity mostly remain zero and only shows a change when the hydrofoil is performing the stroke reversal. The concept of synchronization can also be applied between the hydrodynamic moment and angular velocity. Since in the case, positive $C_{p\theta}$ is only achieved when C_θ and $\dot{\theta}c/U_\infty$ are synchronized (positive power extraction) at $t/T \approx 0.45$ and 0.90, while for the rest of the flapping motion $C_{p\theta}$ is almost at the zero-line, due to angular velocity being zero for most part of the flapping motion. When adding both C_{ph} and $C_{p\theta}$ together, which has both higher peak values and a positive trend.

For free-stream velocities U_∞ = 0.65 and 0.78 m/s, the decrease in peak values in C_p and larger part of flapping cycle crossing and staying in the red zone (Fig. 8) ($0.177 < t/T < 0.37$ & $0.696 < t/T < 0.856$) is attributed to the lift force-plunging velocity synchronization, since $C_{p\theta}$ profiles are almost similar between the two free-stream velocities cases. Hydrodynamic lift shows a slight increase with increase in free-stream, however C_p shows smaller peaks and energy expenditure behavior due to the de-synchronization between C_h and $\dot{h}/U_\infty$, as already mentioned. Furthermore, when calculating C_p using Eq (10), the common multiplication factor ($1/U_\infty$) decreases from 1.7544 to 1.2821 with increase in U_∞, hence affecting the overall C_p values in a flapping cycle.

Force-motion synchronization is an important aspect in the energy harvesting through flapping motion study and it is inevitable that to achieve a good performance, the hydrofoil must exhibit behavior where hydrodynamic lift and torque are synchronized with plunging and angular velocity, respectively. This cohesion may be affected by several factors, which include flow conditions as discussed. Higher free-stream velocities tend to facilitate unsteadiness and turbulence in the incoming flow, which affected our flow induced (passive) flapping wing energy harvester. The energy harvesting performance degraded when the test-rig was subjected to higher velocities, since we witnessed both force and motion parameters being de-synchronized.

Figure 10 shows the plunging motion data (force, motion and power) and qualitative flow visualization

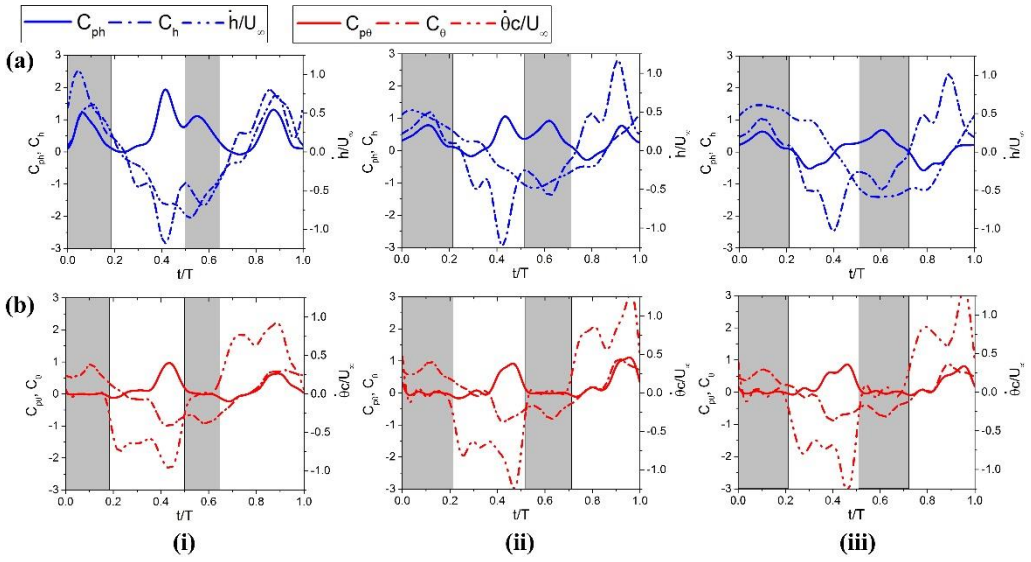

Fig. 9. Plots showing phase-averaged (a) C_{ph}, C_h and $\dot{h}/U_\infty$ and (b) $C_{p\theta}$, C_θ and $\dot{\theta}c/U_\infty$ for flat plate foil at θ_o = 43˚, x_p = 0.65c, m_{ib} = 0.45 kg/block and free stream velocities (i) 0.57 m/s, (ii) 0.65 m/s and (iii) 0.78 m/s.

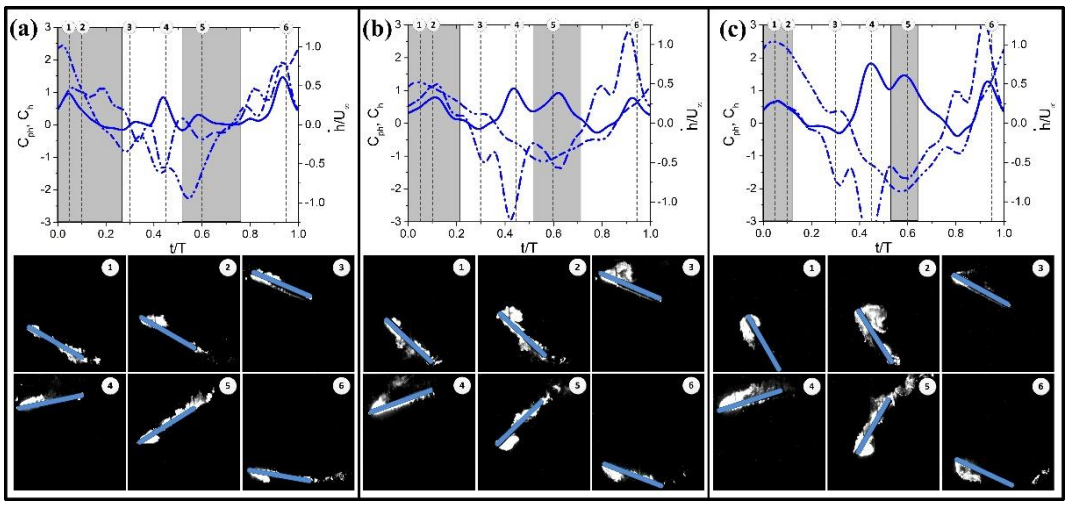

Fig. 10. Laser Induced Fluoresce flow visualization images of a flat plate foil at different time instants marked in their respective graphs consisting of C_{ph}, C_h and $\dot{h}/U_\infty$ data for m_{ib} = 0.45 kg/block, x_p = 0.65c, U_∞ = 0.65 m/s at pitching amplitudes, (a) 30˚, (b) 43˚ and (c) 60˚.

data for different pitching amplitudes at x_p = 0.65c, m_{ib} = 0.45 kg/block and U_∞ = 0.65 m/s. The graphs are also marked with six distinct time stamps at which the flow visualization pictures are shown. In Fig. 7 we saw an increase in energy extraction performance ($\bar{C}_p$) as the pitching amplitude increased while keeping the free-stream velocity fixed. This is supported by the trend exhibited in Fig. 10, where peaks in C_{ph} shows an increase as the pitching amplitude is increased. As already established before, total energy (C_p) follows C_{ph} trend and $C_{p\theta}$ only enhances the energy extraction performance during the last stage of stroke reversal (occurring only twice during the flapping cycle), as shown in Fig. 11.

The peaks in C_{ph} in Fig. 10 (a) are occurring not only during final stroke reversal, but also during the pure plunging motion when the flat plate foil is at its maximum pitching amplitude. With the foil being at an angle with reference to the incoming free-stream, it forms a separation region on its suction side (up during upstroke and down during downstroke). This separation region allows the flow to circulate which leads to the formation of a Leading-Edge Vortex or LEV. This LEV starts to form up when the foil initiates its plunging motion and continues its growth as the foil accelerates. This formation of LEV leads to an increase in hydrodynamic lift and as the LEV grows and travels on the flat plate foil, it eventually sheds and disperses into the wake causing the hydrodynamic lift force to decrease. The size of LEV is determined on the size of the separation area, which would only increase as the pitching amplitude increases, as seen in flow visualization plots in Fig.

10. This increase will eventually cause the hydrodynamic lift to be higher than at smaller pitching amplitudes. Figure 10 exhibits the same trend as the pitching amplitude increases, where C_h shows increase, especially during the pure plunging phase. With good synchronization with their respective $\dot{h}/U_\infty$, which also show an increase with increasing pitching amplitude, C_{ph} increases. Higher pitching amplitudes also increase the hydrodynamic torque and angular velocity and we can see improvement in $C_{p\theta}$ peaks (Fig. 11). Together, C_{ph} and $C_{p\theta}$ increase the C_p peaks which lead to higher $\bar{C}_p$.

From Fig. 7 we also observe (for varying θ_o at x_p = 0.65c, m_{ib} = 0.45 kg/block and U_∞ = 0.65 m/s) that the contribution from $C_{p\theta}$ increases with increasing pitching amplitude, however C_{ph} still contributes more than $C_{p\theta}$ at each θ_o. The higher percentage contribution at lower pitching amplitudes by plunging motion may be attributed to the portion of the flapping cycle spent for translational motion at fixed pitching amplitude. In Fig. 10, plots are marked with gray areas, which refer to the time range where the flat plate foil plunges while at maximum set pitching amplitude.

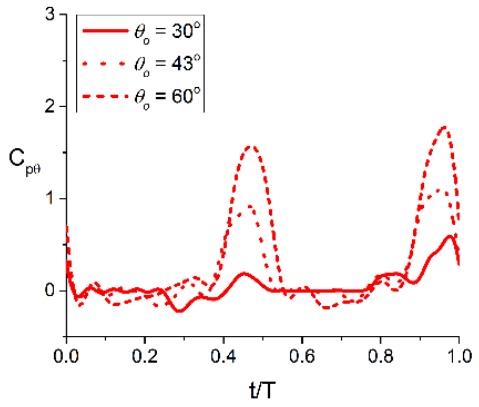

Fig. 11. Phase-averaged $C_{p\theta}$ for flat plate foil at U_∞ = 0.65 m/s, x_p = 0.65c and m_{ib} = 0.45 kg/block for θ_o = 30˚, 43˚ and 60˚.

A detailed explanation regarding the gray and white regions marked in the plots has been discussed earlier. Time ranges differ at each θ_o, where they decrease considerably with increasing θ_o ($0 < t/T < 0.27$ & $0.52 < t/T < 0.76$ for θ_o = 30˚ compared to $0 < t/T < 0.11$ & $0.53 < t/T < 0.64$ for θ_o = 60˚), which is most likely due to the increase in plunging velocity. With the considerable increase in C_h due to the LEV formation and shedding and its good synchronization with $\dot{h}/U_\infty$, we observed considerable improvement in energy harvesting performance.

3.3 Effect of Linear Inertia on Test-Rig Performance

Effect of different inertial mass units on the energy harvesting performance of this test-rig is discussed in this section. Force and motion data and their synchronization factor are taken into consideration in order to explain any kind of trend as the inertial mass unit is increased. As explained earlier, the inertial mass units not only serve as a supporting mechanism to allow the hydrofoil to perform stroke reversal (pitching motion) at the end of each plunging stroke, but also serve as a passive load system which can affect the kinetics of a flow-induced flapping foil energy harvester.

The case-set to be discussed in this section is flat plate foil subjected to three different inertial mass blocks (m_{ib}); Small (0.45 kg/block), Baseline (0.90 kg/block) and Big (1.35 kg/block) at U_∞ = 0.57 m/s, θ_o = 60˚ and x_p = 0.65c. As observed in detail in the previous section, we saw that the flat plate foil in this test-rig gave better energy harvesting performance at lower free-stream velocities during the water speed analysis and at higher pitching amplitudes in the pitch amplitude effect study. This is also evident in the summarized performance metric shown in Fig. 7. Although due to the passive (flow-induced) nature of our test-rig, the system has shown different trends through different combinations of pitching amplitudes and free-stream velocities as the inertial mass is linearly increased. However, analyzing the conditions in which the system performed better will help us understand the trend in detail with the help of force-motion data. Additionally, this paper provides a baseline to fully understand the test-rig and the concept of passively actuated flapping foil energy harvester and lay the foundation for our upcoming publications.

Figure 12 shows the stacked column plot for variation of C_p (which includes C_{ph} and $C_{p\theta}$ marked with blue and red color bars respectively) with variation in the inertial mass unit. In addition, Fig. 13 shows the phase-averaged C_p data for the three inertial mass units.

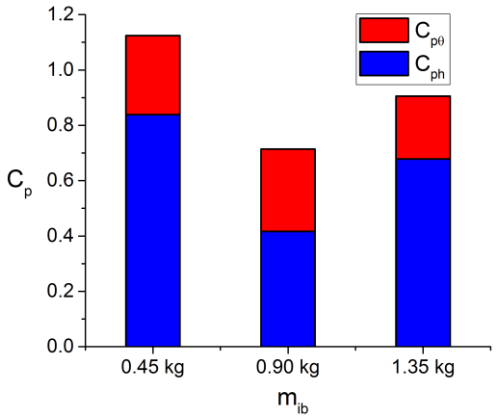

Fig. 12. Figure showing stacked column configuration of $\bar{C}_p$ for a flat plate foil at U_∞ = 0.57 m/s, θ_o = 60˚ and x_p = 0.65c for Small (0.45 kg/block), Baseline (0.90 kg/block) and Big (1.35 kg/block) inertial mass units (m_{ib}) The blue bars represent the contribution by the plunging motion ($\bar{C}_{ph}$) and red bars by the pitching motion ($\bar{C}_{p\theta}$) to the total energy harvesting at each inertial mass unit.

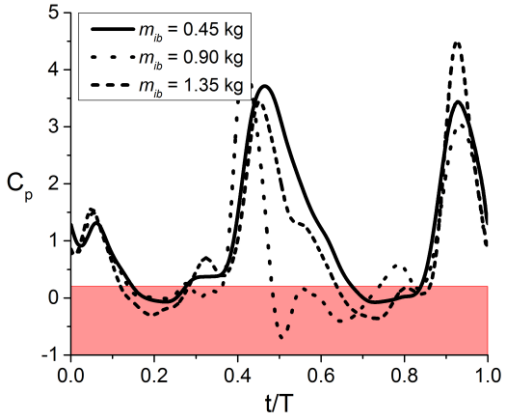

Fig. 13. Figure showing C_p plots for a test-rig configured at θ_o = 60˚, U_∞ = 0.57 m/s and x_p = 0.65c and subjected to three different inertial mass units (m_{ib}). The lightly shaded red region shows the area of energy expenditure by the system rather than extracting energy from the free-stream.

From Fig. 13 we can see that the first smaller peak at $t/T \approx 0.05$ are almost the same for all three inertial mass block units. Since the pitching amplitude, free-stream velocity and pivot location are the same, due to which the hydrodynamic lift is generated as a result of LEV formation and shedding is almost similar, as shown in Fig. 14. The second peaks occurring at approximately $t/T \approx 0.43$ are although at approximately the same level but the instant from which they increase and then decrease is different. C_p values increase at almost the same instant ($t/T \approx$ 0.35), however m_{ib} = 0.45 kg/block and 1.35 kg/block show a gradual decrease after they reach the peak value of $C_p \approx 3.5$ at $t/T \approx 0.43$. C_p for both inertial mass configurations continue to decline till $t/T \approx 0.66$ until they cross the energy expenditure region (red zone in Fig. 13) for a short duration ($0.66 < t/T < 0.85$). Comparatively, C_p in m_{ib} = 0.90 kg/block case takes a sharp decline after $t/T \approx 0.43$ and goes into the energy expenditure zone at $t/T \approx$ 0.465, where it stays there till $t/T \approx 0.75$ loosing energy to the surrounding fluid. As the flat plate foil undergoes a second stroke reversal after $t/T \approx 0.65$ (for all inertial mass unit configurations as shown in Fig. 14) we observe a second peak at $t/T \approx 0.93$ which shows the flat plate foil completing its stroke reversal and touching the pitching limiter.

The trend in C_p observed in Fig. 13 can be explained by looking at the cohesion between the force and torque generated by the flat plate foil when subjected to incoming free- stream flow and their respective kinematics, which together convert it to energy extracted from the surrounding fluid.

Figure 14 shows the C_{ph}, C_h, $\dot{h}/U_\infty$ (Fig. 14 (a)) and $C_{p\theta}$, C_θ and $\dot{\theta}c/U_\infty$ (Fig. 14 (b)) of a flat plate foil at θ_o = 60º, x_p = 0.65c and U_∞ = 0.57 m/s. C_h for all three inertial mass units are very much similar to each other, which is due same pitching amplitude of 60° set. Furthermore, the higher pitching amplitude leads to the formation of a large separation area and eventually the onset of LEV and its subsequent shedding from the foil's surface. As a result, during pure plunging motion at constant θ_o, we see a peak in C_h in the grey shaded regions (Fig. 14 (a)). Although the flat plate foil is subjected to the same free-stream velocity, the difference in inertial mass does affects the plunging velocity of the system as can be seen in Fig. 14 (a). For m_{ib} = 0.90 kg/block, $\dot{h}/U_\infty$ is comparatively higher than the other inertial mass blocks, however the synchronization between C_h and $\dot{h}/U_\infty$ is affected especially during the downstroke phase of the flapping cycle ($t/T > 0.5$). As we observed in Fig. 13, there was considerable loss of energy by the system and C_p remains negative from $t/T \approx 0.465$ to $t/T \approx 0.75$, which is also the case for C_{ph} in Fig. 14 (a-ii). We have already established in the previous section that most of the contribution towards the total energy harvested is from the plunging motion and C_p always follows its respective C_{ph}, which we are also witnessing here. This is also supported by the stacked column figure given in Fig. 12. For other inertial mass block systems (m_{ib} = 0.45 kg/block and 1.35 kg/block) C_{ph} remains in the positive sphere ($C_{ph} > 0$) for almost the whole flapping cycle, and only goes near zero during the early to mid-stroke reversal phase, owing to the good synchronization between C_h and $\dot{h}/U_\infty$. Additional peaks occurring in the white region around $t/T \approx 0.45$ and $t/T \approx 0.93$ is because of the flat plate foil finishing its stroke reversal and striking the pitching limiter, which is recorded by the force sensor as a spike in its force and moment measurements.

Figure 14 (b) shows the force-motion and energy harvesting due to pitching motion and we observe a common trend as seen in our previous discussions. Pitching motion augments to the total energy extraction by the system at two singular points during a flapping cycle, i.e. at the end of the stroke reversal, while it remains zero during the rest of the flapping cycle. $C_{p\theta}$ profiles for all three inertial mass units looks similar (peak values within a small range of $C_{p\theta\text{-}peak} \approx$ 1.50-1.60 at $t/T \approx 0.485$ & 0.95 for all three m_{ib} cases), however there is a subtle difference in the angular velocity profile and the subsequent C_θ generated by the hydrofoil during the flapping motion. With increasing inertial mass (m_{ib} = 0.45 kg/block → 0.90 kg/block → 1.35 kg/block), there is a slight decrease in C_θ, however $\dot{\theta}c/U_\infty$ is comparatively higher for m_{ib} = 0.90 kg/block, with m_{ib} = 1.35 kg/block closer to the former inertial mass and lowest in the m_{ib} = 0.45 kg/block case.

The reason for higher angular velocities at larger inertial blocks is due to the higher mass of the blocks allowing more momentum to the flat plate foil during the pitching motion, although plunging velocity tends to decrease gradually as more inertial load is added to the system. Even so, due to the almost similar ratio of C_θ and $\dot{\theta}c/U_\infty$ among the three inertial mass configurations, $C_{p\theta}$ observes similarities among the three configurations as a result. This is also evident from the red bars in Fig. 12 representing $\bar{C_{p\theta}}$, which are almost the same indicating that contribution towards total energy harvesting through pitching motion is almost equal as the inertial mass is increased.

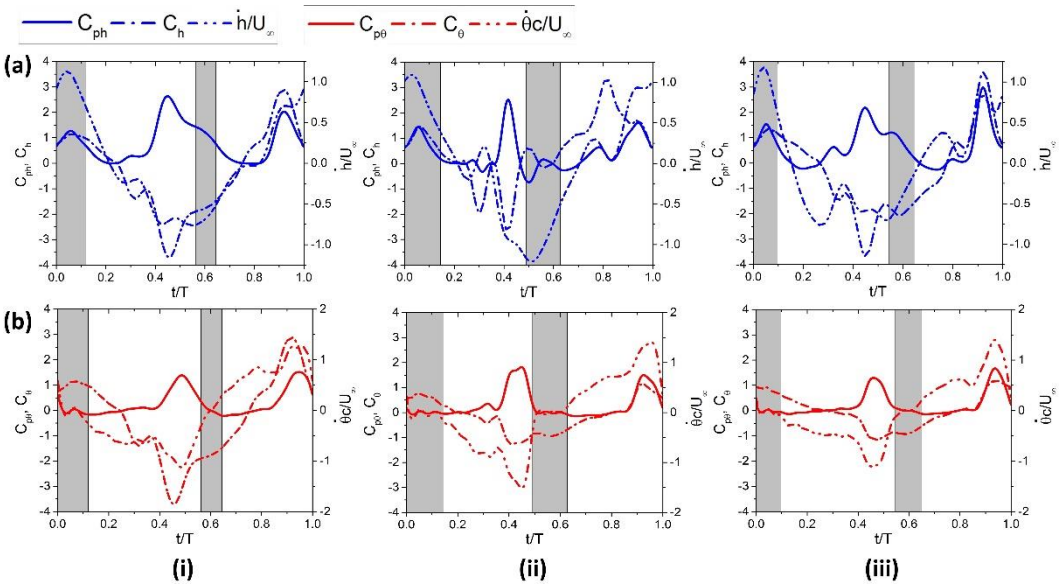

Fig. 14. Plots showing phase-averaged (a) C_{ph}, C_h and $\dot{h}/U_\infty$ and (b) $C_{p\theta}$, C_θ and $\dot{\theta}c/U_\infty$ for flat plate foil at θ_o = 60°, x_p = 0.65c, U_∞= 0.57 m/s and inertial mass unit blocks (m_{ib}) (i) 0.45 kg/block, (ii) 0.90 kg/block and (iii) 1.35 kg/block.

3.4 Performance Comparison with other Works

The different activation mechanisms through which energy can be harvested from incoming free stream have been defined in Section 1. Our literature survey of such mechanisms indicated that most of the focus has been given to fully active and semi active systems, due to their ease of their implementation in both experimental and computational studies, leading to detailed parametric analysis, where some of these have already been discussed in Section 1. A few experimental studies involving fully passive energy harvesting systems have been conducted such as by Kinsey *et al*. (2011), Semler (2009), Platzer & Bradely (2009), McKinney & DeLaurier (1981) etc however their studies didn't focus on the detailed fluid-structure interaction (FSI) analysis which can provide a perspective to energy harvesting performance when subjected to real flows while some such as of McKinney & DeLaurier (1981), Davids and Jones *et al.* (1999) and Kinsey *et al.* (2011), involved complex mechanical systems forcing the foil to move in one way when subjected to incoming free stream.

Table 1 shows a summarized comparative analysis of our energy harvesting performance with some of the major experimental and some computational works in the literature. Most of the studies as seen in Table 1 have been conducted using the symmetrical NACA series foils while, this study (2018), Semler (2010), Usoh *et al.* (2012) have worked on flat plate foil while Zhu (2012) on 12% thick Joukowsky foil. Higher *Re* is also considered in the analysis by most researchers while a few have worked on *Re* = 1100 as shown in Table 1. Since, our test-rig didn't have

any complex mechanical system to induce a specific kinematic motion nor phasing between the plunging and pitching motion as compared to the other fully passive experimental campaigns, therefore the motion and the resulting forces were fully determined by the incoming free-stream. This allowed our system to generate higher energy harvesting performance as compared to other studies given in the Table 1. This result was followed by Kinsey *et al*. (2011) and Young *et al*. (2013) where they achieved 40 and 41% energy harvesting performance (efficiency), respectively. It can also be observed that by changing the foil shape to flat plate foil may have contributed towards higher energy harvesting performance in our case. However, a detailed FSI analysis of foil morphology effect on flapping wing energy harvesting performance is required to support this. The table also indicates that by changing the motion profile from sinusoidal to non-sinusoidal improved the energy harvesting performance, which can be corroborated by extensive studies conducted in this domain by Xiao *et al*. (2012) and Young *et al*. (2013).

4. CONCLUSION

We have presented in this paper an unexploited area in the domain of energy harvesting through flapping wings, i.e. flow induced or passively flapping foil energy harvesters. Unlike previous computational and experimental campaigns focusing on fully active and semi-active flapping foil energy harvesters, the flapping foil in a passive flapping energy harvester is dependent on the incoming free-stream to let it operate. To achieve that, the system requires a minimum threshold free-stream velocity, which can provide the necessary force to allow it to perform flapping motion. Such was the case in our experiments, where after careful design, fabrication and configuration testing the cutoff-velocity

Table 1 Comparison of energy harvesting performance of different computational and experimental studies versus this study

Type of Study	Author/Year	Foil Geometry	Kinematics & *Re*	Activation Mechanism	$\bar{C}_p$	η
Experimental	This Study/ 2018	Flat plate	Non-sinusoidal 7.6×10^4-1.09×10^5	Fully Passive	1.124	52.45%
	McKinney & DeLaurier/1981	NACA0012	Sinusoidal 8.5×10^4-1.1×10^5	Fully Passive	0.14	17%
	Davids, Jones et al./1999	NACA0012	Sinusoidal 2.2×10^4-4.7×10^4	Fully Passive	0.19	16%
	Simpson et al./ 2008	NACA0012	Non-Sinusoidal 1.38×10^4	Fully Prescribed	Not Given	32%
	Semler/2010	Flat plate	Non-Sinusoidal 4.9×10^4-1.9×10^5	Fully Passive	Not Given	
	Abiru & Yoshitake/2011	NACA0015	Sinusoidal 5.0×10^4	Semi-Active	Not Given	22%
	Kinsey et al./2011	NACA0015	Sinusoidal 5.0×10^5	Fully Passive	1.02	40%
	Huxham et al./2012	NACA0015	Sinusoidal 4.5×10^4	Semi-Active	Not Given	24%
	I. Fenercioglu et al./2014	NACA0012	Non-Sinusoidal 1100	Fully Active	0.86	33%
Computational	Usoh et al./2012	Flat plate	Sinusoidal 1100	Fully Active	0.87	34%
	Zhu/2012	12% thick Joukowsky	Variable 1000	Fully Passive	Not Given	31%
	Young et al./2013	NACA0012	Non-Sinusoidal 1100 & 1.1×10^6	Fully Passive	1.10	41%

achieved (without sensors) was 0.37 m/s, while for test-rig fully equipped with sensors was 0.50 m/s.

Free-stream velocity, pitching amplitude and inertial mass block load effects on the energy harvesting performance of our passively actuated flapping energy harvester were discussed at fixed x_p of 0.65c. While keeping pivot location, inertial block mass and pitching amplitude constant, we observed that with increasing free-stream velocity energy harvesting performance ($\bar{C}_p$) decreased, especially at higher pitch amplitudes. We also observed that most of the contribution towards total energy harvesting was through plunging motion ($\bar{C}_{ph}$), while pitching motion would only contribute at two instants during the flapping cycle; at the end of its stroke reversal. In the pitching amplitude study, we observed that by keeping the flat plate foil at higher pitching amplitude, the separation region would grow. As the foil would plunge (up or down), the circulation of the flow on the foil's suction side would lead to the formation of a vortex in the separation region leading to the generation of high lift. This lift would increase as the LEV grows and takes a sudden decline as the LEV moves past the pivot point on the foil's suction side and sheds into the wake. With the generation of high lift force and plunging velocity and their subsequent good synchronization leads to better energy extraction performance.

The overall best performance among these two studies was achieved by the flat plate foil at U_∞ = 0.57 m/s and $\theta_o = 60^\circ$ at x_p = 0.65c achieving a $\bar{C}_p$ of 1.124 and η of 52.46%. Effect of varying mass of inertial blocks on the energy harvesting performance of the test-rig were also studied, where the mass blocks would act as a load. Analysis was done using the parameters in Section 3.2 which gave better energy harvesting performance results ($\theta_o = 60^\circ$ and U_∞ = 0.57 m/s) and varied the mass of the inertial blocks linearly (m_{ib} = 0.45 kg/block, 0.90 kg/block and 1.35 kg/block). It was found that the test-rig is sensitive to changes in load and flow conditions. This affected the force-motion cohesion which is the pinnacle of energy harvesting. m_{ib} = 0.90 kg/block didn't have good synchronization between its C_h and $\dot{h}/U_\infty$ due to which it lost its energy to the fluid, especially during the downstroke phase (t/T > 0.5). For m_{ib} = 0.45 kg/block and 1.35 kg/block configuration, they had comparatively better cohesion between their C_h and $\dot{h}/U_\infty$ due to which C_{ph} and eventually C_p for these two configurations were mostly positive during the flapping cycle.

5. FUTURE WORK

Future work will focus on the quantitative analysis including Particle Image Velocimetry (PIV) and subsequent detailed fluid-solid interaction of flat plate foil in a flow induced energy harvesting environment. Other parametric studies will include pivot location variation, coupled effect of pitching amplitude and pivot location, foil morphology and ground effects on the energy harvesting performance. A detailed analysis of the current test-rig theoretical model is also in progress. All these will provide a better foundation for studies focusing on passive flapping foil energy harvesters in the future.

ACKNOWLEDGEMENTS

M. N. Mumtaz Qadri would like to thank The Hong Kong Polytechnic University for providing the

scholarship to conduct this research leading to the PhD degree.

REFERENCES

Ashraf, M. A., J. Young, J.C.S. Lai and M.F. Platzer (2011). Numerical Analysis of an Oscillating Wing Wind and Hydropower Generator. *AIAA Journal* 49 (7), 1374-1386.

Dumas, G. and T. Kinsey (2006). Eulerian simulations of oscillating airfoils in power extraction regime. *Advances in Fluid Mechanics* VI, WIT, 245-254.

Hisanori, A. and Y. Akira (2012). Experimental Study on a Cascade Flapping Wing Hydroelectric Power Generator. *Journal of Energy and Power* 6, 1429-1436.

Isogai, K. and H. Abiru (2012). Study of Multi-Wing Configuration of Elastically Supported Flapping Wing Power Generator. *Trans. Japan Society Aeronautical and Space Sciences* 55(2), 133-142.

Kinsey, T. and G. Dumas (2008). Parametric Study of an Oscillating Airfoil in a Power Extraction Regime. *AIAA Journal* 46(6),1318-1330.

Kinsey, T., G. Dumas, G. Lalande, J. Ruel, A. Mehut, P. Viarouge, J. Lemay and Y. Jean (2011). Prototype testing of a hydrokinetic turbine based on oscillating hydrofoils. *Renewable Energy* 36(6), 1710 -1718.

McKinney, W., and J. DeLaurier (1981). The Wingmill: An Oscillating Wing Windmill. *Journal of Energy,* AIAA 5(2),109-115.

Peng, Z. and Q. Zhu (2009). Energy Harvesting through flow induced oscillations of a foil. *Physics of Fluids* 21(12), 123601-123609.

Platzer, F. M., M. A. Ashraf, J. Young and C. S. J. Lai (2009). Development of a New Oscillating-Wing Wind and Hydropower Generator. *47th AIAA Aerospace Sciences Meeting. Orlando, Florida:* 1-13.

Platzer, M. F. and R. A. Bradley (2009). Oscillating-wing power generator with flow induced pitch-plunge phasing. *I. C. A. D. F. U. C. U. Patent.*

Poirel, D., F. Mendes (2011). Experimental investigation of small amplitude self-sustained pitch-heave oscillations of a NACA0012 airfoil at transitional Reynolds numbers. *Proceedings of the 50th AIAA Aerospace and Science Meeting*. Nashville, Tennessee.

Poirel, D., Y. Harris and A. Benaissa (2008). Self-sustained aeroelastic oscillations of a NACA0012 airfoil at low-to moderate Reynolds numbers. *Journal of Fluids and Structures*24, 700–719.

Poirel, D., Y. Harris, A. Benaissa (2006). Aeroelastic dynamics of a NACA 0012 airfoil in the transitional Reynolds number regime. *Summer Conference of the ASME Pressure Vessels and Piping Division. Vancouver, Canada.* Paper PVP2006-ICPVT11-93957, 847-854.

Semler, C. S., *Experimental Investigation of an Oscillating Flow Generator*, MSc Thesis, U.S. Naval Postgraduate School, Monterey, CA, 2010.

Shimizu, E., K. Isogai, and S. Obayashi (2008). Multi objective Design Study of a Flapping Wing Power Generator. *Journal of Fluids Engineering* 130.

Simpson, B. J., F. S. Hover and M. S. Triantafyllou (2008a). Experiments in direct energy extraction through flapping foils. *In: Proceedings of the Eighteenth International Offshore and Polar Engineering Conference*. July 6–11, Canada.

Simpson, B. J., S. Licht, F. S. Hover and M. S. Triantafyllou (2008b). Energy extraction through flapping foils. In: *Proceedings of 27th International Conference on Offshore Mechanics and Arctic Engineering*, OMAE-2008-58043.

Usoh, C. O., Young, J., Lai, J. C. S. and Ashraf, M. A. (2012). Numerical Analysis of a Non-Profiled Plate for Flapping Wing Turbines. *In: Proceedings of the 18th Australasian Fluid Mechanics Conference AFMC*, Launceston, Australia.

Xiao, Q., W. Liao, S. Yang and Y. Peng (2012). How motion trajectory affects energy extraction performance of a biomimic energy generator with an oscillating foil. *Renewable Energy* 37(1), pp. 61-75.

Yonghui, Xie., Lu Kun., and Zhang Di., (2014). Investigations on energy extraction performance of an oscillating foil with modified flapping motion. *Renewable Energy* 63, 550-557.

Young, J., M.A. Asharf, J.C.S. Lai and M.F. Platzer (2013). Numerical Simulation of fully passive flapping foil power generation. *AIAA J* 51(11), 2727-2739.

Zhu, Q. (2012). Energy harvesting by a purely passive flapping foil from shear flows. *J Fluids Struct* 34, 157-169.